Novel Thin-Film Nanocomposite Forward Osmosis Membranes Modified with WS$_2$/CuAl LDH Nanocomposite to Enhance Desalination and Anti-fouling Performance

Mojtaba Bagherzadeh[1] · Mohammad Nikkhoo[2] · Mohammad Mahdi Ahadian[2] · Mojtaba Amini[3]

Abstract
Designing efficient membranes for desalination to help reduce the water shortage crisis has been the subject of various studies. In this study, first, CuAl LDH nanosheets were prepared and the surface of some thin-film composite (TFC) membranes was modified by them. Afterward, the novel heterostructure nanocomposite consisting of CuAl LDH and WS$_2$ nanosheets was synthesized by hydrothermal method, and a new kind of thin-film nanocomposite (TFN) membranes were made using them. All the obtained membranes performance was studied in the forward osmosis (FO) process. The effects of the prepared compounds on the morphology, chemical structure, hydrophilicity, and topology of the polyamide (PA) active layer were evaluated by scanning electron microscopy (SEM), FT-IR spectroscopy, energy-dispersive X-ray (EDX), powder x-ray diffraction (XRD), water contact angle (WCA) goniometer and atomic force microscope (AFM) analysis. Finally, by comparing the results for both types of modified membranes, the membrane containing 0.025 wt% of the nanocomposite modifier showed the highest water flux (29.30 LMH) and selectivity (0.38 g/L) that was chosen as the optimal membrane. Also, the anti-fouling properties of this membrane were studied and the obtained results showed an increase in the fouling resistance compared to the membrane without filler.
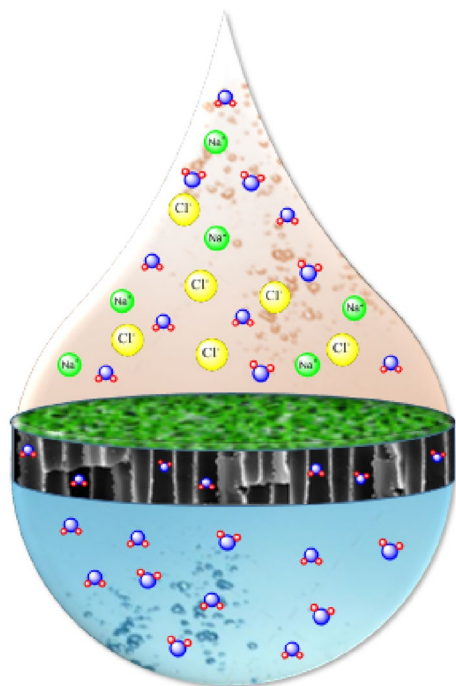
✉ Mojtaba Bagherzadeh
  bagherzadeh@sharif.edu

1   Chemistry Department, Sharif University of Technology,
    P.O. Box 11155-3615, Tehran, Iran

2   Institute for Nanoscience and Technology, Sharif University
    of Technology, Tehran, Iran

3   Department of Inorganic Chemistry, Faculty of Chemistry,
    University of Tabriz, Tabriz, Iran

Graphical Abstract

Keywords Forward osmosis · Transition metal dichalcogenides · layered double hydroxides · Thin-film nanocomposite membrane · Desalination

1 Introduction

According to various reports, more than half of the world's population is facing some form of water shortage, which is due to the world's growing population as well as global warming. Water scarcity can negatively affect more and more people and regions around the world [1–4]. Although most of our planet's surface is covered by water, a significant amount of this water is not usable for humans, and only 3% of the freshwater resources are suitable for human needs [5]. Given these conditions and an increase in water demands, it is necessary to adopt appropriate methods to bridge the water demand gap. Forward osmosis is one of these emerging methods that has received more attention in recent years due to its merits [6, 7]. In this system, there is a semi-permeable membrane that separates a solution with low osmotic pressure (feed solution) from one with high osmotic pressure (draw solution). The concentration difference of the solutions between the two sides of the membrane affords the difference in osmotic pressure and causes the water molecules to enter the draw solution spontaneously in the opposite direction of the osmotic pressure gradient. [8, 9] Because of the fundamental role that the membrane plays

in the FO system, fabricating membranes with high permeability and selectivity is one of the most important goals that researchers pursue. In addition, a number of features such as low fouling tendency, low cost, convenient cleaning, high chemical stability, and mechanical strength can make a membrane more practical [10–12].

Nanomaterials are a good option for surface modification of thin-film composite membranes if they have such properties as high surface area, porosity, antimicrobial features, and hydrophilicity. In these membranes, polyethersulfone (PES) is usually used as a supporting layer and its surface is coated with polyamide in the interfacial polymerization (IP) process [13]. One of the common methods to modify the surface of these membranes is to add nanomaterials in the IP step, in which case the nanomaterials can be placed on the surface of the membrane and its nearby [14–16]. The presence of nanomaterials in the active polyamide layer can affect the performance of the membrane. Depending on its structural properties, the nanomaterial may add new properties to the membrane and improve its previous function.

Layered double hydroxides are a group of clays with the general formula $[M^{2+}_{1-x} M^{3+}_{x} (OH)_2] (A^{n-})_{x/n}.mH_2O$, in which M^{2+} and M^{3+} are metal cations and A^{n-} is the interlayer anions [17, 18]. Due to the positive charges of the layers, the interlayers demonstrate a high capacity for anion exchange, which has led to the use of LDHs in various fields such as catalysis, adsorbents, inorganic fillers, supercapacitors, water oxidation, and drug delivery[19–24]. Properties such as hydrophilicity, mechanical strength, and thermal stability make the LDH nanosheets a suitable option for use in the structure of membranes in the FO process [25]. Furthermore, their easy synthesis methods and their low production cost have resulted in researchers' great tendency to use these compounds [26].

Because of the excellent performance of two-dimensional nanomaterials in the field of separation and filtration, these materials have attracted special attention in recent years [27, 28]. Given their suitable hydrophilicity, high surface area, and tunable layer distance, 2D nanosheets as graphene oxide (GO) and graphene have been used for desalination, water purification, oil/water separation, and anti-fouling coating [29–34]. Transition metal dichalcogenides (TMDs) are another group of 2D materials that have the ability to improve desalination performance in the FO process because of their excellent separation capability, hydrophilicity, multifunctionality, and anti-fouling properties [35]. Based on simulation and experimental studies, MoS_2 membranes have shown promising results due to their high rigidity, few defects, and low hydraulic resistance [36]. In the TMDs' structures, each layer of the transition metal is surrounded on both sides by chalcogen atoms, and therefore forms a three atomic structure that provides the TMDs nanosheets with rigidity and uniform hydrophilicity. Moreover, there

is more water penetration through 2D TMDs-based membranes than through GO membranes. The water permeance through reported TMDs laminar membranes was 2–5 times higher than that through GO membranes due to their high surface smoothness without any oxygen-containing functional groups [37, 38].

In the present study, CuAl LDH nanosheets were synthesized by the hydrothermal strategy. Afterward, a WS$_2$/CuAl LDH nanocomposite was prepared by electrostatic self-assembled chemistry, using an in situ hydrothermal method. The TFC membranes were modified separately by various concentrations of synthesized compounds. In addition, this study aimed to investigate the effect of the presence of obtained compounds in the active layer on hydrophilicity, surface porosity, morphology, water permeation, salt rejection, and fouling resistance of the membranes. The fabricated thin-film nanocomposite (TFN) membranes were tested on a laboratory scale to evaluate their performance in the FO process. Because of the properties mentioned for both compounds, we assume that modifying the surface of a membrane by the WS$_2$/CuAl LDH nanocomposite could improve its performance in both water permeability and salt rejection.

2 Experimental Section

2.1 Materials and Chemicals

Copper(II) nitrate trihydrate (Cu(NO$_3$)$_2$.3H$_2$O), aluminium nitrate nonahydrate (Al(NO$_3$)$_3$·9H$_2$O), sodium tungstate (Na$_2$WO$_4$), thiourea (SC(NH$_2$)$_2$), urea (CO(NH$_2$)$_2$) polyethylene glycol 300 (PEG-300), m-phenylenediamine (MPD), trimesoyl chloride (TMC), N,N-dimethylformamide (DMF), n-hexane, dimethyl sulfoxide (DMSO), ammonium chloride (NH$_4$Cl), sodium bicarbonate (NaHCO$_3$), magnesium sulfate (MgSO$_4$), monopotassium phosphate (KH$_2$PO$_4$) and calcium chloride (CaCl$_2$) were purchased from Merck Co. Polyethersulfone (Ultrason® E 6020, MW: 58,000) obtained from BASF Co. Sodium hydroxide (NaOH) and sodium alginate (SA) were obtained from Sigma Aldrich Co. Sodium chloride (NaCl) obtained from Iranian Salts Companies. Ethanol was purchased from Scharlau Co.

2.2 Preparation of Cu–Al LDH

In order to synthesize of Cu–Al LDH, the previously reported hydrothermal procedure was used [39]. 9 mmol of Cu(NO$_3$)$_2$.3H$_2$O was dissolved in a mixture of 45 mL deionized water and 15 mL DMSO, and then, 4.5 mmol of Al(NO$_3$)$_3$.9H$_2$O was added to the previous solution and stirred until clear. Afterward, the urea was added to the prior solution at 0.2 mol/L. The resulting solution was stirred until

a clear solution formed. In the following, the obtained solution was poured into a 100 mL Teflon-lined autoclave and maintained at 110 °C for 12 h. The resulting sky blue powder was collected by centrifuging, washed with distilled water and ethanol several times and finally, dried at 100 °C for 12 h.

2.3 Preparation of WS$_2$/CuAl LDH Nanocomposite

2 mmol of Cu(NO$_3$)$_2$.3H$_2$O and 1 mmol of Al(NO$_3$)$_3$.9H$_2$O were dissolved in 10 mL of deionized water and sonicated for 30 min to obtain a clear solution. The pH of the solution was adjusted to 9 using the aqueous solution of NaOH (5.07 g, 10 mL), in which case LDH was converted to a jelly state. Then the resulting product was added to a mixture of water (25 mL) and ethanol (75 mL) and dispersed for 30 min. In another beaker, 1 mmol of Na$_2$WO$_4$ and 5 mmol of thiourea were poured into distilled water (60 mL) and ethanol (20 mL) and the prepared solution was sonicated for 30 min, then stirred for 30 min. At this step, the prepared WS$_2$ precursor in the previous step was added dropwise to the transparent gel dispersion of CuAl LDH with constant stirring and the resulting suspension was stirred for another 1 h. The obtained mixture was poured into a Teflon-lined autoclave and heated at 260 °C for 24 h. The synthesized product was collected using a centrifuge, and then washed with deionized water, and ethanol and finally dried at 60 °C [40]. The synthesis process of WS$_2$/CuAl LDH nanocomposite is illustrated in Fig. S1 in the Supporting Information.

2.4 Preparation of PES Support Membrane

The porous PES flat sheet is prepared as a support for the thin-film composite membrane by a phase inversion process. Briefly, the solution required to fabricate the PES substrate was obtained by dissolving 2 g of PES in a mixture of 5.6 g of PEG and 11.2 g of DMF at room temperature. The final solution was kept stationary until the air bubbles inside it were removed. Afterward, the prepared solution was cast on a flat glass plate using a casting knife (thickness = 120 μm). In the next step, to initiate the phase inversion process the glass was placed in a water bath at room temperature. The formed membranes were stored in deionized (DI) water until any modification [41].

2.5 Preparation of the TFC and TFN Membranes

To prepare the TFC membrane, the PES membrane made in the previous step entered the interfacial polymerization stage by MPD and TMC monomers. The surface of the PES was reacted with an aqueous solution of MPD (2 wt%) for 2 min and after separating the excess MPD from the surface, the organic solution of TMC (0.15 wt%) was added to the

surface of the treated membrane and kept for 1 min. Finally, the polyamide layer was fabricated as the active layer on the obtained membrane by placing it at 70 °C for 5 min. TFN membranes were prepared seperately by adding Cu–Al LDH and WS$_2$/CuAl LDH to the aqueous solution during the IP process using the same TFC fabrication method. All the TFN membranes made with different concentrations of modifiers are summarized in Table S1 (see Supporting Information).

2.6 Characterization of Cu–Al LDH, WS$_2$/CuAl LDH and Membranes

The FTIR spectra of Cu–Al LDH and WS$_2$/CuAl LDH were recorded in KBr pellets with an Unicam Matson1000 Fourier transform infrared spectrophotometer in the region of 400–4000 cm^{-1}. Moreover, the FTIR spectra of membranes were obtained using PerkinElmer, Spectrum TWO LiTa, UK Attenuated total reflectance − Fourier transform infrared (ATR − FTIR) spectrometer over the range of 500 –4000 cm^{-1}. X-ray diffraction (XRD) patterns were obtained using the XPERT-PRO diffractometer (MPD PAN-alytical Company), which has a Cu Kα radiation source. All samples morphologies were imaged with a scanning electron microscope (SEM, Tescan MIRA3). Also, the elemental analysis was performed with energy dispersive X-ray spectroscopy (EDX). The tunneling electron microscopic image was obtained using the Ziess EM900.The surface topography of the synthesized membranes was evaluated using atomic force microscopy (AFM, Park Systems XE 100, Santa Clara, California, USA). The water contact angles were measured using the sessile drop method. The surface charge of sample measured by Meloren ZN Series. The gravimetric method was generally used to calculate the porosity of the prepared support layer[42].

2.7 FO Performance Evaluation

The performance of the prepared membranes was evaluated in two modes, FO (active layer faced feed solution) and PRO (active layer faced draw solution), using a laboratory-scale FO system at room temperature (Fig S2 in the Supporting Information). DI water and salt solution with different concentrations of NaCl (0.5, 1 and 1.5 M) were used as feed and draw solution, respectively. The flow rate on both sides of the filtration cell was set at 150 mL/min and the effective membrane area was 4.15 cm^2. Membranes performance was monitored for salt passage using a calibrated conductometer in the feed solution. At least three repeatability tests were done for each membrane and the average of the obtained results was reported.

Water flux (J$_w$, L/m^{2}h, abbreviated as LMH) was calculated using Eq. 1 in which ΔV (L), Δt (h) and A$_m$ (m^2) are the volume of permeated water, permeation time and membrane's effective area, respectively.

$$J_w = \frac{\Delta V}{A_m \times \Delta t} \tag{1}$$

Equation 2 was used to calculate salt reverse flux (J$_s$, g/m^{2}h, abbreviated as gMH), where C$_f$ and C$_i$ represent the final and initial concentration of NaCl at the feed solution and V$_f$ and V$_i$ are the final and initial feed volumes, respectively.

$$J_S = \frac{\left(C_f V_f - C_i V_i\right)}{A_m \times \Delta t} \tag{2}$$

2.8 Anti-fouling Performance Assessment

The fouling experiment was performed by the FO system on a laboratory scale under FO mode to investigate the anti-fouling properties of TFC and optimized TFN membranes. In this experiment, SA (500 ppm) and 1 M NaCl were used as foulant and draw solution, respectively. First, the FO system was cleaned by circulating DI water on both feed and draw sides for 15 min. Then, synthetic wastewater solution (9.2 mM NaCl, 0.93 mM NH$_4$Cl, 0.5 mM NaHCO$_3$, 0.61 mM MgSO$_4$, 0.45 mM KH$_2$PO$_4$, and 0.5 mM CaCl$_2$) free from foulant as feed solution and 1 M NaCl as draw solution were exerted. An aqueous solution of SA (500 mg/L) was used as organic fullant The SA-free feed solution was used to eliminate the dilution of the draw solution baseline water flux (J$_0$). Then, the dynamic water flux (J$_t$) was measured by adding SA to the feed solution and starting the fouling phenomenon. These fouling tests were performed for 5 h at room temperature.

3 Results and Discussion

3.1 Characterization of Cu–Al LDH and WS$_2$/CuAl LDH

The chemical structure of Cu–Al LDH nanosheets was investigated using FTIR spectroscopy. As shown in Fig. 1a, the broad peak in the region of 3000–3600 cm^{-1} indicates the stretching vibration of the O-H bond of the hydroxides present in the LDH structure as well as the interlayer water molecules. Furthermore, their bending vibrations have appeared at 1614 cm^{-1} [43]. The strong absorption peak at 1376 cm^{-1} is related to the v$_3$ vibration mode of interlayer nitrate anions and the v$_1$ and v$_2$ vibrations of nitrate ions are also weakly noticeable at 1050 and 825 cm^{-1} [44]. The absorption peaks related to the lattice vibration modes of
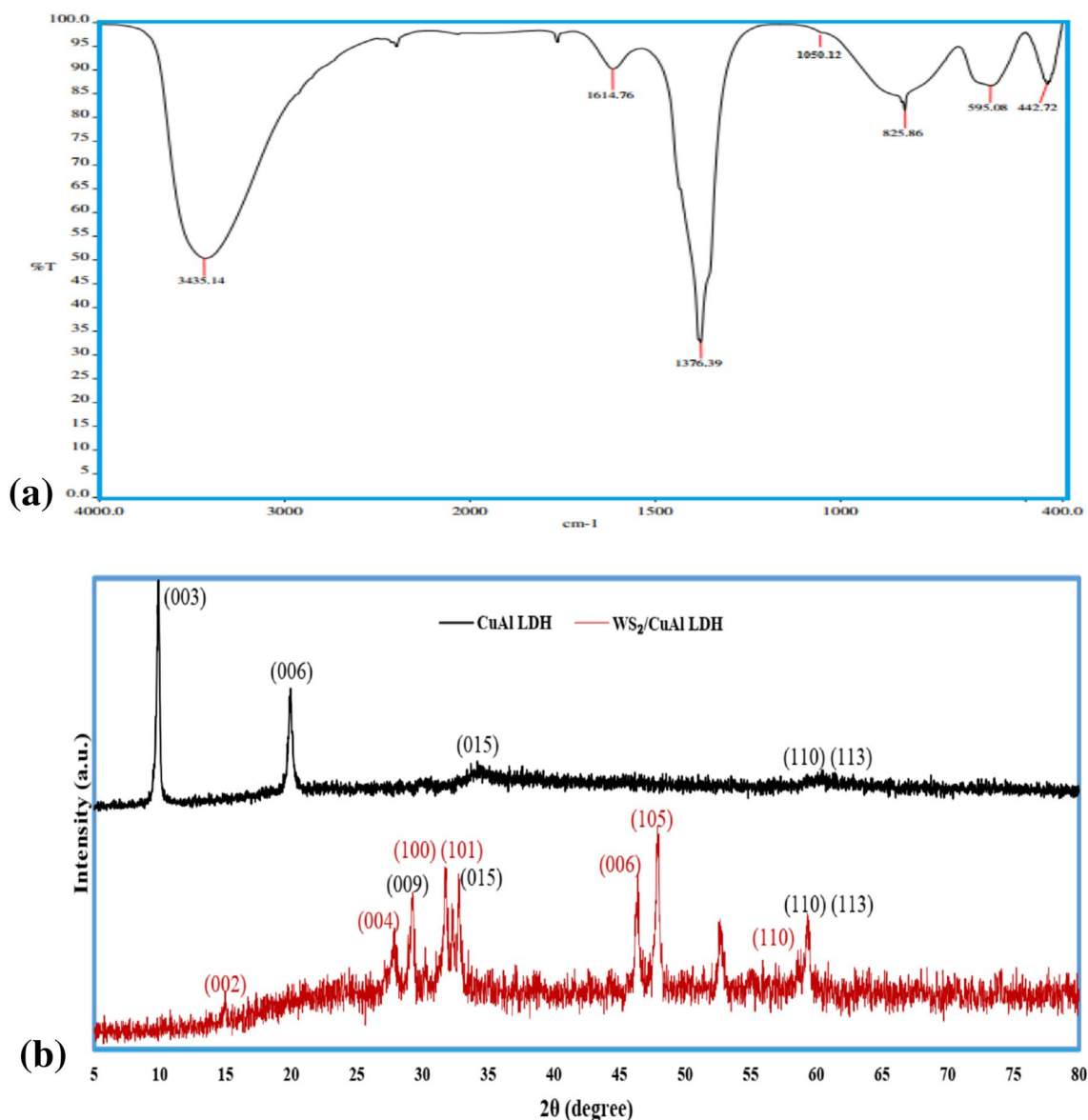
Fig. 1 **a** FTIR spectra of CuAl LDH, **b** XRD pattern of CuAl LDH and WS$_2$/CuAl LDH.

M–O and O–M–O in the LDH sheets are observed in the low frequency region (400–1000 cm^{-1}) of the spectra [45].

The powder XRD pattern of Cu–Al LDH is shown in Fig. 1b. The sharp peaks at 9.8° and 19.9° correspond to (003) and (006) planes. These peaks confirm the layer structure for LDH. Also, the weak and broad reflections at 34.5°, 59.8° and 60.3° related to the diffraction of the (015), (110) and (113) planes. According to the XRD pattern, it can be asserted that the synthesized sample has a crystalline structure and high purity in which there are no impurities [46, 47].According to the XRD pattern of WS$_2$/CuAl LDH illustrated in Fig. 2a, the diffraction peaks observed in the 14.9, 27.8, 31.8, 32.2, 46.3, 47.8 and 58.8 could be assigned into the reflection planes of (002), (004), (100), (101), (006),

(105) and (110) of WS$_2$ nanosheet (red peaks) [48]. The shift of some peaks like (100), (101) and (105) to lower angles compared to the solitary sample demonstrates that the distances between the crystalline layers have increased. Also, due to the very low intensity of the (002) peak, it seems that the few-layered structure of WS$_2$ is formed [49–51]. The peaks in the regions of 29.2, 32.7, 59.3 and 60.8 indicate the presence of CuAl LDH nanosheets in the final product (black peaks). These peaks are assigned into the basal reflection planes of (009), (015), (110) and (113) respectively. Compared to the pure LDH pattern, diffraction planes such as (003) and (006) have been removed and (009) has appeared. Also, the peak intensity of planes such as (015), (110) and (113) has obviously increased. These
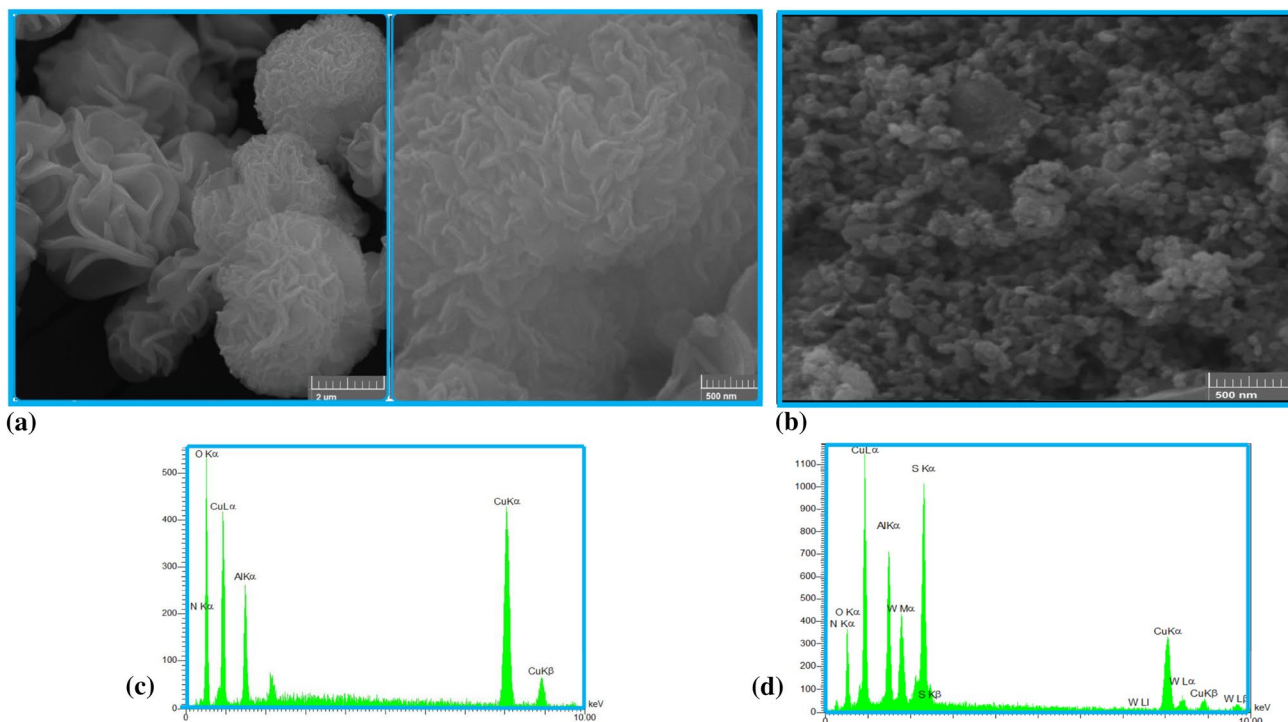
Fig. 2 **a**, **b** SEM images and **c**, **d** EDX elemental spectrum of CuAl LDH and WS$_2$/CuAl LDH.

results portend the formation of CuAl LDH with a good crystalline structure.

The scanning electron microscopy images shown in Fig. 2a were used to investigate the morphology of the Cu–Al LDH nanosheets. The images clearly show that the LDH have a flower-like morphology. This morphology is the result of the irregular and random arrangement of nanosheets and shows its layered structure. In this case, due to the hierarchical structure, interconnected networks of macropores can be formed between LDH layers [39]. In addition, the presence of the Cu and Al peaks in the energy-dispersive X-ray spectrum confirmed the correct synthesis of the nanosheets (Fig. 2c). Figure 2b depicts a SEM image of WS$_2$/CuAl LDH, the hexagonal flaky nanosheets of WS$_2$ on the LDH sheets are marked on the image. The results show that both compounds prevented agglomeration of each other and also both have diameters ranging from 50 to 100 nm. According to the EDX spectrum of WS$_2$/CuAl LDH shown in Fig. 2d, W, S, Al, Cu and O are present in the structure of the prepared nanocomposite and are evidence of its correct synthesis.

Figure 3a shows TEM image of the WS$_2$/CuAl LDH, in which the hexagonal nanosheets of the WS$_2$ and LDH are well defined. Also, nanosheets have been synthesized in a thin form with dimensions below 100 nm and are segregated and without agglomeration. The surface charges of the prepared nanocomposite were investigated by measuring the zeta potential (Fig. 3b). According to previous reports, the surface charge of pristine WS$_2$ is negative and that of LDH is very positive [52, 53], however, the surface charge of their hybrid has been found to be positive (18.7 mV) in this research.

3.2 Membrane Characterization

The FTIR spectrum of TFC, TFN-WL$_1$, TFN-WL$_2$ and TFN-WL$_3$ are demonstrated in Fig. 4a. PES specific peaks are observed in all membranes, which bands at the wavenumbers of 1577, 1485, 1317, 1242 and 1151 cm^{-1} are related to the presence of stretching vibrations of aromatic ring C=C, asymmetric stretching of C–C, C–SO$_2$–C stretching, C–O stretching and C–SO$_2$–C symmetric stretching in the support layer [54, 55]. Also, the presence of peaks 1650 and 1545 cm^{-1} in the spectrum of all membranes, which are related to C=O stretching and N–H bending vibrations shows the formation of a polyamide layer as the active layer on the PES [56, 57]. The stretching modes of N–H and O–H groups on polyamide and nanocomposite appear as a weak and broad peak at 3300–3500 cm^{-1}. Due to the overlap of the nanocomposite peaks with the substrate as well as its low loading at the PA layer, no obvious difference was detected between the TFC and TFN spectra in the lower wavelengths, but by comparing the 3300–3500 cm^{-1} region in the modified membranes and TFC spectra, the peak intensity
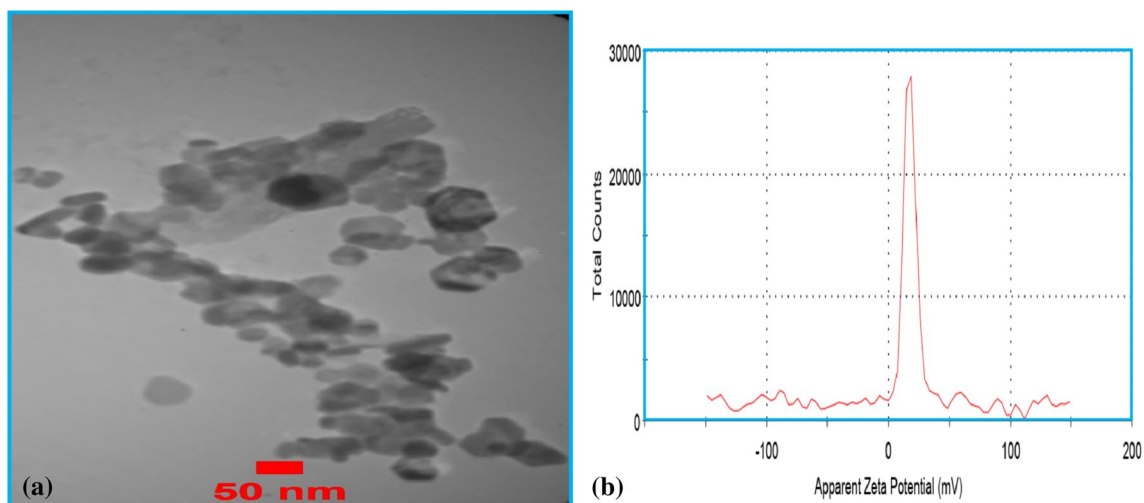
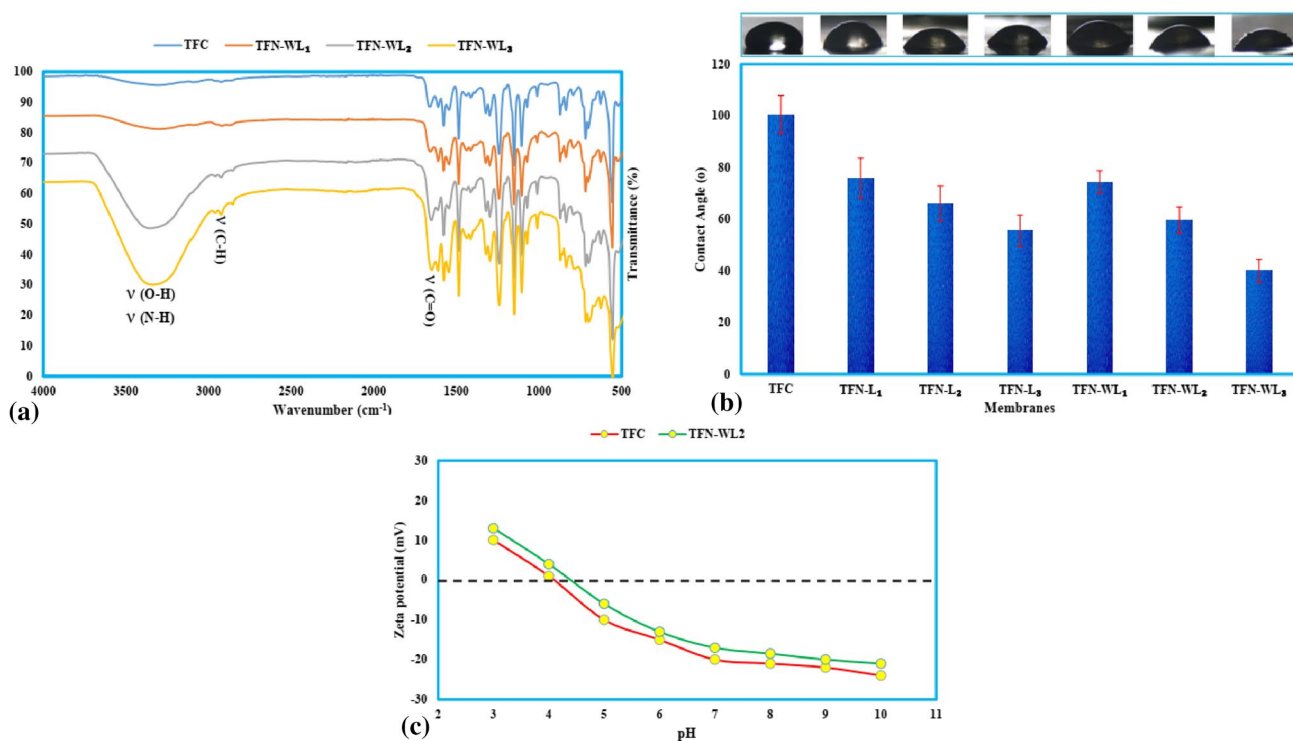**Fig. 3** **a** TEM image and **b** Zeta potential analysis of WS_2/CuAl LDH.

Fig. 4 **a** FTIR spectra of the TFC and TFN-WL, **b** Water contact angle of the TFC and TFN and **c** Zeta potential analysis of the TFC and TFN-WL_2 membranes

increases with increasing filler concentration, which may indicate the presence of nanocomposite O–H groups.

Figure 4b shows the water contact angle data, based on which the hydrophilic properties of the membrane surface can be investigated. By comparing TFC and all TFN membranes, a decrease in the water contact angle was observed in all TFN membranes, which indicates an increase in the hydrophilicity of the membrane's surface. In the TFN membranes modified with CuAl LDH nanosheets, the increase in surface hydrophilicity can be attributed to OH groups in the structure of LDH layers. This affinity for water molecules can be explained by the hydrogen bond interaction between the hydroxide groups and the water molecules. Increasing the loading of the LDH on the surface of these membranes

has reduced the water contact angle regularly so that the contact angle of the TFC has reached from 100.4° to 55.5° for the TFN-L$_3$ membrane. The process of decreasing the water contact angle with increasing the concentration of nanocomposite on the surface is also true for TFN-WL membranes. Due to the presence of homogeneous and hydrophilic layers of S atoms in the structure of WS$_2$, it was expected that their composition with LDH fillers would increase hydrophilicity, which was proved by the results obtained for TFN-WL membranes. The water contact angle of TFN-WL$_3$ membrane compared to TFC and TFN-L$_3$ membranes decreased from 100.4° and 55.5° to 40°, respectively.

The surface charge profiles of the TFC and TFN-WL$_2$ membranes as a function of pH are shown in Fig. 4c. The potential curve of both membranes has the same trend and starts from positive values at low pH and tends to negative values as the pH increases. Due to the presence of carboxylic acid groups on the surface of the active layer, TFC membrane has a negative potential [58]. By adding WS$_2$/CuAl LDH nanocomposite to the surface of the membrane, the potential values at different pH have increased slightly and become more positive compared to TFC membrane. Considering that all the membrane tests were done in the FO process at neutral pH, so the value of the potential in this environment is more important for us. It can be seen that at this pH, the pure nanocomposite has a positive potential (Fig. 3b), and adding it to the surface of the membrane reduced a small amount of the negative potential of the membrane and did not have a significant effect on the potential value.

The top surface morphology of the TFC and all TFN-WL membranes was investigated by SEM images shown in Fig. 5a. Due to the observation of typical ridge-and-valley structure on the TFC surface, the formation of the polyamide layer through IP step on the support layer can be confirmed [59]. With increasing the concentration of the WS$_2$/CuAl LDH on the surface of the modified membranes, the surface folds have also decreased, which can be attributed to the presence of fillers in the active layer and filling the valleys by them [60]. The 3D-AFM images of these membranes are in complete agreement with the results obtained from SEM images. As is clear in the AFM images shown in Fig. 5b, the presence of nanosheets smoothed the surface so that the average roughness (R_a), root-mean-square roughness (R_q) and ten point height (R_{10z}) decreased from 72.01, 92.05 and 867 nm for the TFC to 43.56, 55.83 and 423.0 nm for the TFN-WL$_3$, respectively (see Table S2 in the Supporting Information). The presence of hydroxyl and polar functional groups in the structure of the WS$_2$/CuAl LDH, as well as the formation of hydrogen bonds between nanosheets and MPD monomer can hamper the formation of the PA layer, which causes the membrane to smoothen [61, 62]. Also, EDX spectrums of the TFN-WL membranes show

the presence of Cu, Al, W and S atoms in the membrane structure, which is evidence of the successful modification of the membranes surface by the synthesized nanocomposite (Fig. 5c). Also, the EDX elemental mapping shows the presence of the synthesized nanocomposite and the difference in its loading on the surface of the modified membranes (Fig S3 in the Supporting Information). The cross-section FESEM images showed that the loading of the prepared nanocomposite on the surface of the TFC membrane changed the thickness of its active layer so that the thickness of the active layer decreased from 595 nm for TFC to about 514.8 nm for TFN-WL$_3$. The presence of nanocomposite in the MPD solution prevents the complete reaction of monomers to form polyamide, the reasons for which can be attributed to the formation of hydrogen bonds between them and the MPD monomer, as well as reducing the penetration of MPD molecules towards TMC molecules. As a result, increasing nanocomposite loading will decrease the thickness of the active layer[12]. The results from the cross-sectional images are in agreement with AFM and surface SEM images.

The porosity of the PES support layer was evaluated using the conventional gravimetric experiment. The porosity value for the support layer is 78.2% (± 0.5). Also, the mean pore size is 15.4 (± 0.4) nm. Because in this study, a fixed support layer was used for all membranes and no modification was done on the support layer, the obtained numbers are the same for all membranes.

3.3 FO Performance of the Fabricated Membranes

The performance of the TFC, TFN-L and TFN-WL membranes in the FO process was studied under FO and PRO modes, the results of which are shown in Fig. 6. In order to evaluate the performance of the membranes in both modes, 1 M NaCl was used as a draw solution and DI water as a feed solution. In all membranes, the water flux in the PRO configuration is more than the FO, which according to previous studies is due to the difference in the degree of the concentrative/dilutive ICPs in the two membrane orientations [63, 64]. As can be seen in Fig. 6a, the presence of the CuAl LDH on the surface of the membranes has increased the water flux compared to the TFC membrane, so that by increasing the loading of the LDH to a dosage of 500 ppm (TFN-L$_3$), J_w has reached from 14.45 to 19.30 LMH in the FO mode. This upward trend is also true in the PRO mode. As shown in Fig. 6b, the reverse salt flux also enhanced with increasing J_w in the TFN-L membranes compared to the pristine TFC. According to the results obtained from the water contact angle analysis, the increase in the water flux in these membranes can be attributed to the improvement in hydrophilicity of the LDH-containing membranes. Additional pathways created in the presence of the LDH nanosheets itself can also affect the better performance of
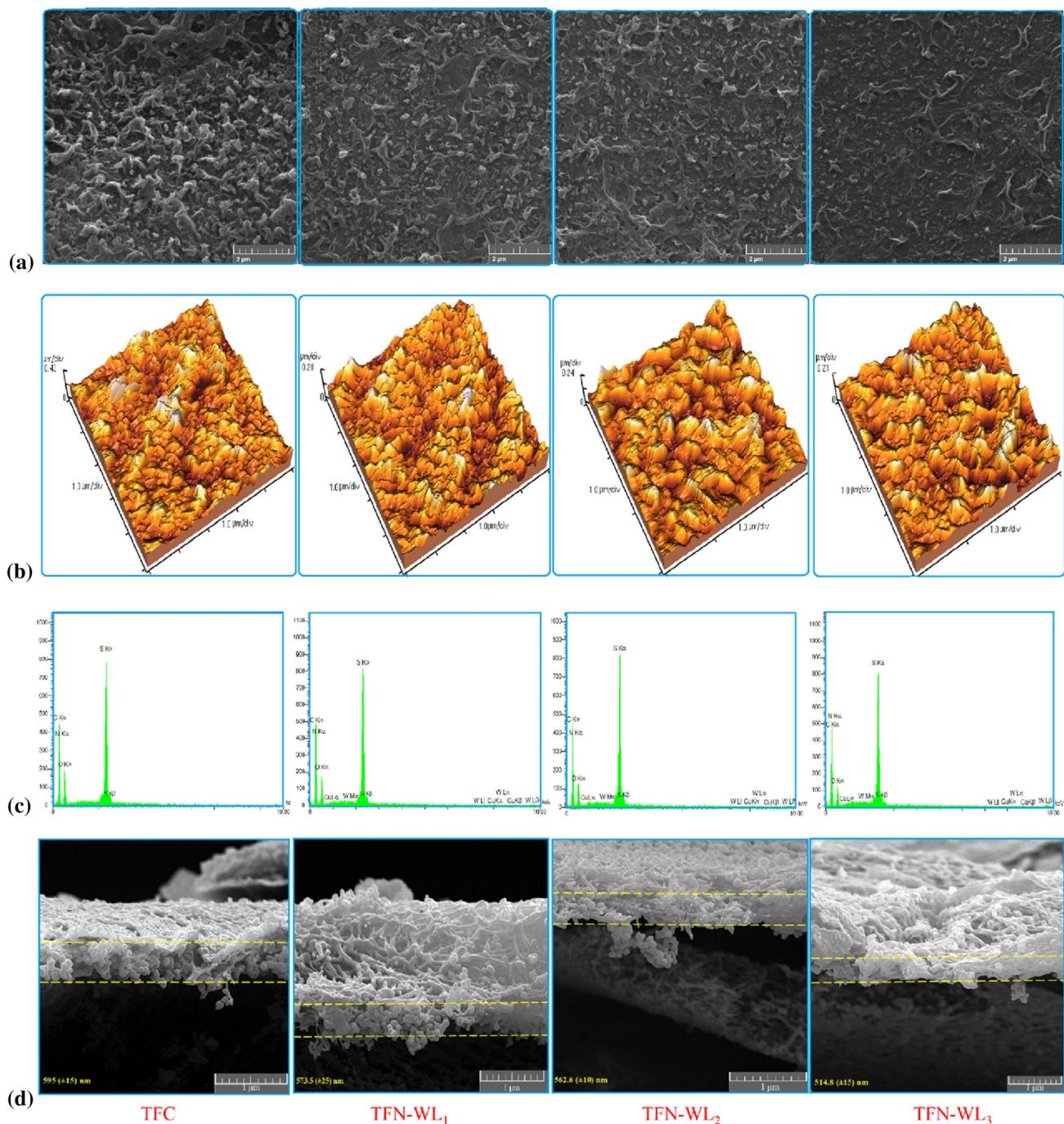
Fig. 5 **a** Surface SEM images (scale bars are 2 μm), **b** 3D AFM images, **c** EDX spectra and **d** cross-sectional FESEM images (scale bars are 1 μm) of the TFC and TFN-WL membranes

the membranes [65, 66]. Membranes modified by WS_2/CuAl LDH have increased water permeability compared to the TFC and TFN-L_3 (the best LDH-modified membrane) so that with the presence of these fillers, the value of J_w from 14.45 to 19.30 LMH for the TFC and TFN-L_3 has reached 29.30 LMH. This amount of water flux was obtained for the TFN-WL_2 membrane, which is the most efficient membrane among the TFN-WL membranes. The addition of the WS_2 nanosheets to the pure LDH structure has significantly improved membrane performance. The high tendency of the surface of the membranes to water molecules in the presence of WS_2 nanosheets can be one of the most important factors. As a result, a layer of water is formed on the membrane surface. This layer absorbs water molecules into the membrane
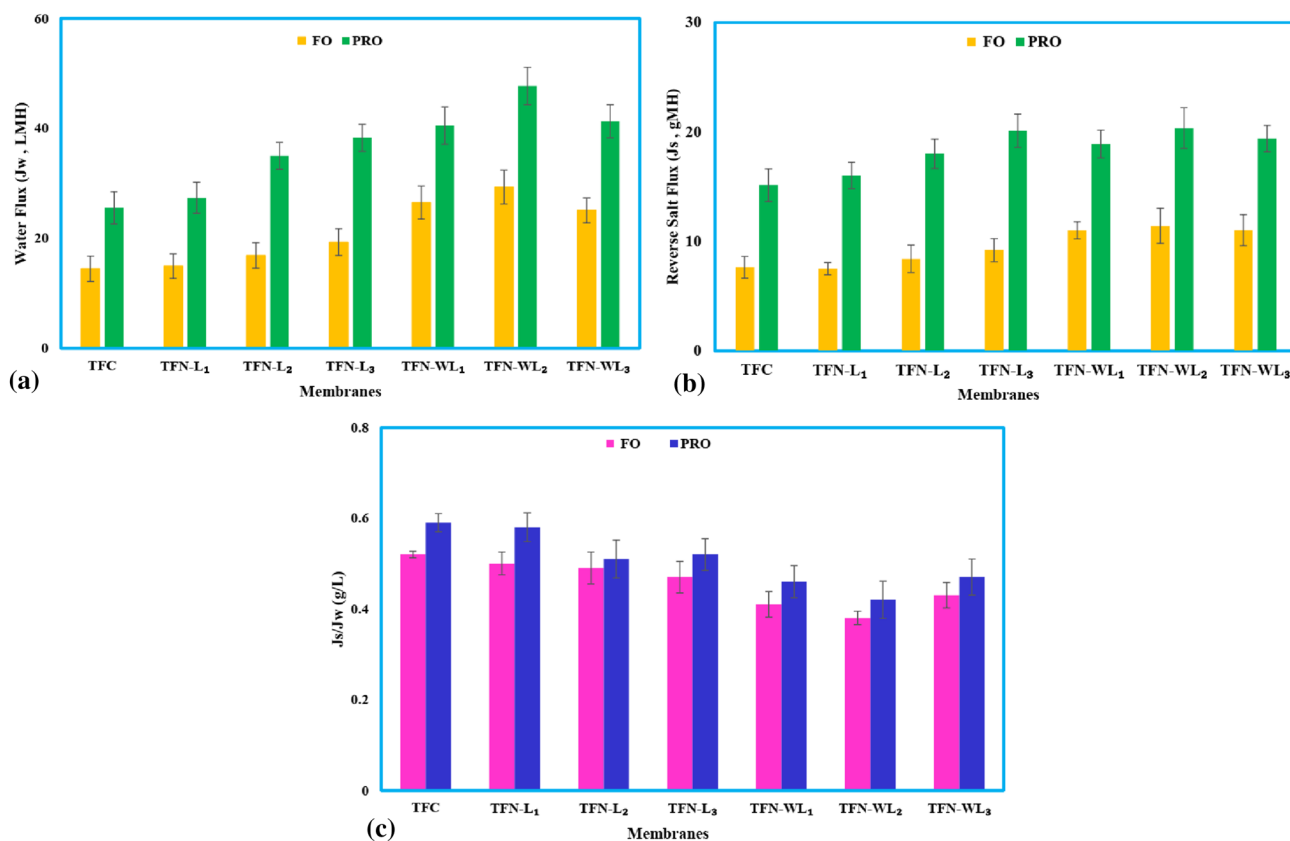
Fig. 6 **a** Water flux, **b** reverse salt flux and **c** Js/Jw ratios of the TFC and TFN membranes in both FO and PRO modes

matrix to provide faster water transfer [67, 68]. Also, according to some reports, the arrangement of WS_2, the fish-bone shaped pore and hydrophilic atoms along with the pore can be effective in the occurrence of these properties. The fish-bone shaped pores are composed of the hourglass-shaped nanopores that have the ability to increase flux and penetrate rates [27, 28]. What is more, overlapping parts of WS_2 nanosheets with each other and with LDH nanosheets can create a lot of empty spaces. These spaces act as nanochannels to transport and separate molecules [35, 38]. All these mentioned mechanisms are possible and proposed mechanisms for the passage of water molecules (Fig S4 in the Supporting Information). As can be seen in Fig. 6, water and reverse salt fluxes for membranes follow a similar trend as reported by other researchers [69, 70]. Although raising the dosage of fillers from 100 to 250 ppm has enhanced the trend of J_w and J_s with different slopes, but increasing the concentration above 250 ppm has decreased the trend. The maximum amount of J_s in the FO and PRO modes is related to the TFN-WL2 membrane with values of 11.42 and 20.35 gMH. The increment in the reverse salt flux is probably due to the increase in pathways and channels in the active layer that has reduced the penetration resistance. The decline in TFN-WL3 membrane performance can be attributed to the

blockage of water influence pathways because of the high concentration of fillers and their agglomeration.

The J_s/J_w parameter is used to select the most efficient membrane in the desalination process, which represents selectivity. In general, the lower the ratio, the higher the membrane efficiency. This parameter is one of the most important characteristics of a suitable membrane and the researchers aim to reduce its value compared to the TFC and other modified membranes. The J_s/J_w is calculated for TFC, TFN-L and TFN-WL membranes and is represented in Fig. 6c. Compared to the TFC, this ratio has decreased for both types of membrane modified with different fillers in the FO and PRO modes. The lowest ratio among CuAl LDH and WS_2/CuAl LDH modified membranes in the FO mode belongs to TFN-L3 and TFN-WL2 membranes with values of 0.47 and 0.38 g/L, which has decreased well compared to TFC membrane (0.52 g/L). Based on the results, the TFN-WL2 membrane showed the best performance at the FO and PRO modes and is the most selective membrane among all fabricated membranes. According to the XRD pattern of the WS_2/CuAl LDH, most of the d-spacing value between the layers corresponds to the (002) peak (0.589 nm). This value is less than the diameter of hydrated Na^+ (0.716 nm) and Cl^- (0.664 nm) ions and also more than the size of water

molecules (0.276 nm), so the factor of the size of water molecules, hydrated ions and d-spacing can be considered as one of the main factors affecting the separation mechanism and its effect on the membrane's selectivity is also quite clear [57].

Figure S5 (see Supporting Information) shows Jw and Js values of the TFC and TFN-WL$_2$ membranes at different concentrations of the draw solution in both FO and PRO modes. Changing the concentration of the draw solution will change the osmotic pressure on both sides of the membrane so that the changes in solution concentration and osmotic pressure are consistent with each other. Therefore, according to the results, increasing the concentration of the solution enhances the water flux and the reverse salt flux has shown a similar trend.

3.4 Anti-fouling Performance of the Membranes

The results of the optimal TFN-WL$_2$ membrane in the fouling test are shown in Fig. 7 in which SA used as the model foulant. In this experiment, 1 M NaCl was used as a draw solution and all tests were performed in the FO mode. As the results show, the performance of both membranes has weakened over time, but the slope of this attenuation is higher for the TFC membrane, which indicates a greater propensity to fouling compared to the modified membrane. The appearance of the anti-fouling property in the TFN-WL$_2$ membrane can be attributed to its hydrophilic and smooth surface in comparison with the control membrane (TFC) [71–73]. The incorporation of the LDH and WS$_2$ hydrophilic layers on the surface of

the membrane increases its hydrophilicity and leads to the formation of a water layer on the surface. Due to the less tendency of the SA to the hydrophilic surface compared to water molecules, this layer of water is formed on the surface in the presence of foulant. On the other hand, surface roughness because of the increase of the foulants adsorption sites has a negative effect on the anti-fouling properties of membranes, which are less present on smooth surfaces [67]. Although the value of the surface potential has become slightly more positive compared to the TFC membrane, and due to the presence of SA as a foulant, this can hurt the anti-fouling properties of the membrane, but the amount of this potential change is not significant, and the factors of the hydrophilicity and surface smoothness have been more effective than the surface charge and able to increase anti-fouling properties. After 5 h of the fouling test, the control membrane showed 31.17% reduction in the water flux, while this value was 22.88% for the optimal membrane.

The performance of the TFC, TFN-WL$_2$ and some of the modified membranes from previous reported studies are summarized in Table S3 (see Supporting Information). Comparison of the performance of the modified membrane in the present work with other studies based on the TFC membrane of each work shows its remarkable efficiency. The TFN-WL$_2$ has a higher water flux than TFN-2, TFN-U2, TFN-0.1 and LDH@TFC-LDH and less than TFN-QMo-2 and TFN-0.25 membranes in the FO mode. Also, the selectivity of the fabricated membrane relative to the TFC has been improved by 27%, which is higher than most of the values reported for other membranes.

Fig. 7 The anti-fouling characteristic of the TFC and TFN-WL$_2$ membranes in FO mode
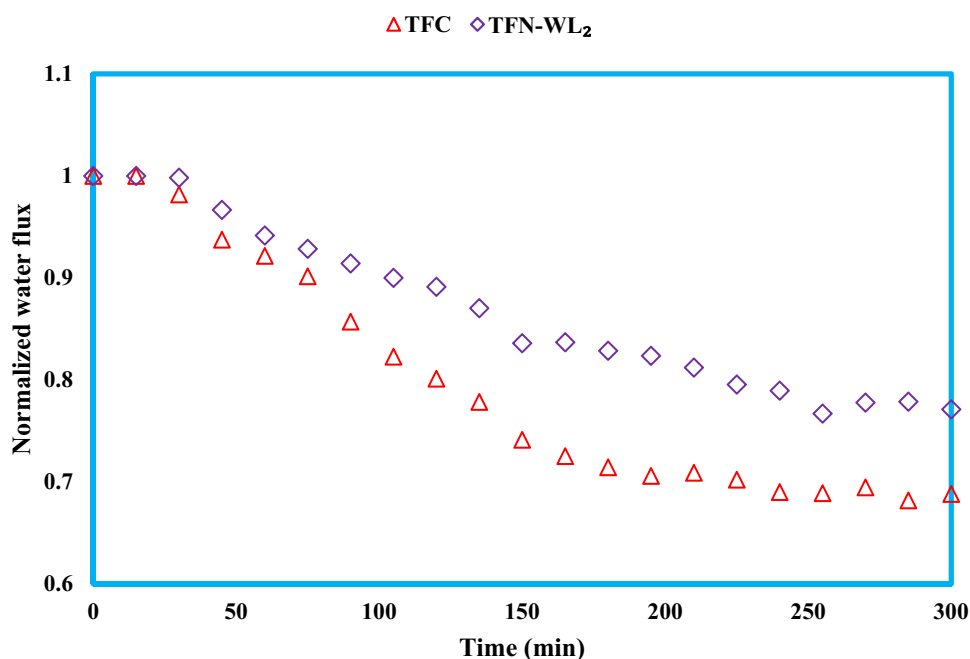
4 Conclusion

The CuAl LDH and WS$_2$/CuAl LDH nanosheets were synthesized and incorporated separately on the surface of the TFC membrane during the IP process. These nanofillers altered the structural and chemical properties of the membranes, which led to an improvement in the desalination by the FO process. In summary, nanocomposite-containing membranes performed better than modified membranes by the pure LDH, the reasons for which can be mentioned as follows: (i) high hydrophilicity of TFN membranes in the presence of WS$_2$ sheets and increasing the tendency of their surface to absorb water molecules (due to the hydrophilic and uniform surface of these sheets) and (ii) the arrangement of WS$_2$ (because of the formation of the fish-bone shaped pores and the hourglass-shaped nanopores with hydrophilic walls and the ability to pass water quickly). Among all the modified membranes, TFN-WL$_2$ had the highest water permeability of 29.30, 47.7 LMH and the best selectivity of 0.38, 0.42 g/L for both FO and PRO modes, respectively. Also, the smoother surface of this membrane compared to the TFC, which was proved by SEM and AFM analysis, caused its anti-fouling properties.

Declarations

Conflict of interest The authors declare that they have no known competing financial interests or personal relationships that could have appeared to influence the work reported in this paper.

References

1. W. Bank, *The Role of Desalination in an Increasingly Water-Scarce World* (World Bank, 2019)
2. C.J. Vörösmarty, P. Green, J. Salisbury, R.B. Lammers, Science **289**, 80-. (2000) 284
3. X. Qu, J. Brame, Q. Li, P.J.J. Alvarez, Acc. Chem. Res. **46**, 834 (2013)
4. M.A. Montgomery, M. Elimelech, Environ. Sci. Technol. **41**, 17 (2007)
5. S. Thatai, R. Verma, P. Khurana, P. Goel, D. Kumar, in *A New Gener. Mater. Graphene Appl. Water Technol* (Springer, 2019), pp. 21–42
6. S. Zhao, L. Zou, C.Y. Tang, D. Mulcahy, J. Memb. Sci. **396**, 1 (2012)
7. N. Akther, A. Sodiq, A. Giwa, S. Daer, H.A. Arafat, S.W. Hasan, Chem. Eng. J. **281**, 502 (2015)
8. P. Lu, Y. Gao, A. Umar, T. Zhou, J. Wang, Z. Zhang, L. Huang, Q. Wang, Sci. Adv. Mater. **7**, 2182 (2015)
9. M. Bagherzadeh, A. Bayrami, M. Amini, J. Water Process. Eng. **33**, 101107 (2020)
10. M. Amini, M. Seifi, A. Akbari, M. Hosseinifard, Polyhedron **179**, 114362 (2020)
11. B. Mi, M. Elimelech, J. Memb. Sci. **348**, 337 (2010)
12. M. Bagherzadeh, A. Bayrami, Z. Shekari, M. Amini, Desalination **515**, 115181 (2021)
13. D.L. Zhao, S. Japip, Y. Zhang, M. Weber, C. Maletzko, T.-S. Chung, Water Res. **173**, 115557 (2020)
14. M.B.M.Y. Ang, Y.-L. Ji, S.-H. Huang, H.-A. Tsai, W.-S. Hung, C.-C. Hu, K.-R. Lee, J.-Y. Lai, J. Memb. Sci. **539**, 52 (2017)
15. N.Y. Yip, A. Tiraferri, W.A. Phillip, J.D. Schiffman, M. Elimelech, Environ. Sci. Technol. **44**, 3812 (2010)
16. H. Choi, A.A. Shah, S.-E. Nam, Y.-I. Park, H. Park, Desalination **449**, 41 (2019)
17. M. Xu, B. Bi, B. Xu, Z. Sun, L. Xu, Appl. Clay Sci. **157**, 86 (2018)
18. R. Pourfaraj, S.J. Fatemi, S.Y. Kazemi, P. Biparva, J. Colloid Interface Sci. **508**, 65 (2017)
19. P. Lu, S. Liang, L. Qiu, Y. Gao, Q. Wang, J. Memb. Sci. **504**, 196 (2016)
20. Q. Wang, D. O'Hare, Chem. Rev. **112**, 4124 (2012)
21. M. Shao, F. Ning, M. Wei, D.G. Evans, X. Duan, Adv. Funct. Mater. **24**, 580 (2014)
22. D. Pan, H. Zhang, T. Fan, J. Chen, X. Duan, Chem. Commun. **47**, 908 (2011)
23. B.M. Choudary, S. Madhi, N.S. Chowdari, M.L. Kantam, B. Sreedhar, J. Am. Chem. Soc. **124**, 14127 (2002)
24. S.J. Kim, Y. Lee, D.K. Lee, J.W. Lee, J.K. Kang, J. Mater. Chem. A **2**, 4136 (2014)
25. Q. Zhao, D.L. Zhao, F. Feng, T.-S. Chung, S.B. Chen, Desalination **527**, 115583 (2022)
26. R. Botan, T.R. Nogueira, F. Wypych, L.M.F. Lona, Polym. Eng. Sci. **52**, 1754 (2012)
27. M. Heiranian, A.B. Farimani, N.R. Aluru, Nat. Commun. **6**, 1 (2015)
28. S. Gravelle, L. Joly, F. Detcheverry, C. Ybert, C. Cottin-Bizonne, L. Bocquet, Proc. Natl. Acad. Sci. **110**, 16367 (2013)
29. Z. Wang, B. Mi, Environ. Sci. Technol. **51**, 8229 (2017)
30. A.K. Mishra, S. Ramaprabhu, Desalination **282**, 39 (2011)
31. S. Zheng, B. Mi, Environ. Sci. Water Res. Technol. **2**, 717 (2016)
32. K. Huang, G. Liu, Y. Lou, Z. Dong, J. Shen, W. Jin, Angew. Chemie **126**, 7049 (2014)
33. M. Hu, S. Zheng, B. Mi, Environ. Sci. Technol. **50**, 685 (2016)
34. Z. Wang, Q. Tu, S. Zheng, J.J. Urban, S. Li, B. Mi, Nano Lett. **17**, 7289 (2017)
35. M.-N. Li, X.-F. Sun, L. Wang, S.-Y. Wang, M.Z. Afzal, C. Song, S.-G. Wang, Desalination **436**, 107 (2018)
36. M.-Q. Ma, C. Zhang, C.-Y. Zhu, S. Huang, J. Yang, Z.-K. Xu, J. Memb. Sci. **591**, 117316 (2019)
37. P. Cheng, Y. Chen, Y.-H. Gu, X. Yan, W.-Z. Lang, J. Memb. Sci. **591**, 117308 (2019)
38. L. Sun, H. Huang, X. Peng, Chem. Commun. **49**, 10718 (2013)
39. J. Li, S. Zhang, Y. Chen, T. Liu, C. Liu, X. Zhang, M. Yi, Z. Chu, X. Han, RSC Adv. **7**, 29051 (2017)
40. S. Nayak, G. Swain, K. Parida, ACS Appl. Mater. Interfaces **11**, 20923 (2019)
41. A. Bayrami, M. Bagherzadeh, H. Navi, M. Chegeni, M. Hosseinifard, M. Amini, Desalination **521**, 115386 (2022)
42. A. Shakeri, S.M.M. Babaheydari, H. Salehi, S.R. Razavi, Langmuir **37**, 7591 (2021)
43. M. Amini, M. Nikkhoo, S.M.F. Farnia, Appl. Organomet. Chem. **31**, e3710 (2017)
44. J.T. Kloprogge, D. Wharton, L. Hickey, R.L. Frost, Am. Mineral. **87**, 623 (2002)

45. M. Nikkhoo, M. Amini, S. Morteza, F. Farnia, A. Bayrami, M. Bagherzadeh, S. Gautam, K.H. Chae, Appl. Organomet. Chem. **32**, e4358 (2018)

46. N.T. Thao, Chem. Eng. J. **279**, 840 (2015)

47. B. Li, Y. Zhao, S. Zhang, W. Gao, M. Wei, ACS Appl. Mater. Interfaces **5**, 10233 (2013)

48. Z. Yuan, Q. Jiang, C. Feng, X. Chen, Z. Guo, J. Electron. Mater. **47**, 251 (2018)

49. H. Hwang, H. Kim, J. Cho, Nano Lett. **11**, 4826 (2011)

50. Q. Wang, J. Li, J. Phys. Chem. C **111**, 1675 (2007)

51. S. Iqbal, Z. Pan, K. Zhou, Nanoscale **9**, 6638 (2017)

52. I.J. Mphahlele, S.P. Malinga, L.N. Dlamini, Catalysts **12**, 504 (2022)

53. V.P. Nguyen, K.T.T. Nguyen, L.T. Ton, D.T. Nguyen, K.Q. Nguyen, M.T. Vu, H.N. Tran, J. Nanomater. 2020, (2020)

54. S. Hadadpour, I. Tavakol, Z. Shabani, T. Mohammadi, M.A. Tofighy, S. Sahebi, J. Environ. Chem. Eng. **9**, 104880 (2021)

55. S. Zhu, S. Zhao, Z. Wang, X. Tian, M. Shi, J. Wang, S. Wang, J. Memb. Sci. **493**, 263 (2015)

56. X. Song, Y. Zhang, H.M. Abdel-Ghafar, E.-S.A. Abdel-Aal, M. Huang, S. Gul, H. Jiang, Chem. Eng. J. **412**, 128607 (2021)

57. M. Bagherzadeh, A. Bayrami, M. Amini, Appl. Organomet. Chem. **34**, e5339 (2020)

58. P. Lu, S. Liang, T. Zhou, T. Xue, X. Mei, Q. Wang, Desalination **421**, 99 (2017)

59. B. Khorshidi, T. Thundat, B.A. Fleck, M. Sadrzadeh, RSC Adv. **5**, 54985 (2015)

60. M. Wu, T. Ma, Y. Su, H. Wu, X. You, Z. Jiang, R. Kasher, J. Memb. Sci. **544**, 79 (2017)

61. A. Shakeri, R. Razavi, H. Salehi, M. Fallahi, T. Eghbalazar, Appl. Surf. Sci. **481**, 811 (2019)

62. H. Salehi, A. Shakeri, H. Naslhajian, M. Amini, J. Polym. Res. **26**, 48 (2019)

63. G.T. Gray, J.R. McCutcheon, M. Elimelech, Desalination **197**, 1 (2006)

64. T.Y. Cath, A.E. Childress, M. Elimelech, J. Memb. Sci. **281**, 70 (2006)

65. H. Dong, L. Wu, L. Zhang, H. Chen, C. Gao, J. Memb. Sci. **494**, 92 (2015)

66. M.H. Tajuddin, N. Yusof, N. Abdullah, M.N.Z. Abidin, W.N.W. Salleh, A.F. Ismail, T. Matsuura, N.H.H. Hairom, N. Misdan, J. Taiwan. Inst. Chem. Eng. **97**, 1 (2019)

67. H.C. Bidsorkhi, H. Riazi, D. Emadzadeh, M. Ghanbari, T. Matsuura, W.J. Lau, A.F. Ismail, Nanotechnology **27**, 415706 (2016)

68. X. Wang, C. Wu, T. Zhu, P. Li, S. Xia, Chemosphere **256**, 127099 (2020)

69. P. Lu, W. Li, S. Yang, Y. Liu, Q. Wang, Y. Li, Sep. Purif. Technol. **220**, 231 (2019)

70. A. Shakeri, H. Salehi, F. Ghorbani, M. Amini, H. Naslhajian, J. Colloid Interface Sci. **536**, 328 (2019)

71. K. Zhu, S. Zhang, J. Luan, Y. Mu, Y. Du, G. Wang, J. Memb. Sci. **539**, 116 (2017)

72. X. Lu, L.H. Arias Chavez, S. Romero-Vargas, J. Castrillón, Ma, M. Elimelech, Environ. Sci. Technol. **49**, 1436 (2015)

73. L. Shen, X. Wang, R. Li, H. Yu, H. Hong, H. Lin, J. Chen, B.-Q. Liao, J. Colloid Interface Sci. **505**, 900 (2017)